Helmholtz-Zentrum Geesthacht
Zentrum für Material- und Küstenforschung

Final Draft
of the original manuscript:

Schwaighofer, E.; Rashkova, B.; Clemens, H.; Stark, A.; Mayer, S.:
Effect of carbon addition on solidification behavior, phase evolution and creep properties of an intermetallic Beta-stabilized Gamma-TiAl based alloy
In: Intermetallics (2013) Elsevier

DOI: 10.1016/j.intermet.2013.11.011

Effect of carbon addition on solidification behavior, phase evolution and creep properties of an intermetallic β-stabilized γ-TiAl based alloy

Emanuel Schwaighofer [a,*], Boryana Rashkova [a], Helmut Clemens [a], Andreas Stark [b], Svea Mayer [a]

[a] Department of Physical Metallurgy and Materials Testing, Montanuniversität Leoben, Roseggerstr. 12, A-8700 Leoben, Austria

[b] Institute of Materials Research, Helmholtz-Zentrum Geesthacht, Max-Planck-Str. 1, D-21502 Geesthacht, Germany

[*] Corresponding author. Tel.: +43 3842 4024204; fax: +43 3842 4024202.

E-mail address: emanuel.schwaighofer@unileoben.ac.at (E. Schwaighofer).

Keywords:

Titanium aluminides; High-energy X-ray diffraction; Carbon; Phase diagram; Creep

Highlights:

- Phase diagram and phase fraction evolution of the Ti-43.5Al-4Nb-1Mo-0.1B-C system
- Change in solidification pathway from β- to peritectic solidification with carbon addition
- Macrotextures of cast/HIP microstructures
- Carbon solubility, carbide formation and hardness evolution
- Microstructure, phase evolution and creep properties of a Ti-43.5Al-4Nb-1.5Mo-0.1B-0.5C alloy

ABSTRACT

Improving mechanical properties of advanced intermetallic multi-phase γ-TiAl based alloys, such as the Ti-43.5Al-4Nb-1Mo-0.1B alloy (in at.%), termed TNM alloy, is limited by compositional and microstructural adaptations. A common possibility to further improve strength and creep behavior of such β-solidifying TiAl alloys is e.g. alloying with β-stabilizing substitutional solid solution hardening elements Nb, Mo, Ta, W as well as the addition of interstitial hardening elements C and N which are also strong carbide and nitride forming elements. Carbon is known to be a strong α-stabilizer and, therefore, alloying with C is accompanied by a change of phase evolution. The preservation of the solidification pathway via the β-phase, which is needed to obtain grain refinement, minimum segregation and an almost texture-free solidification microstructure, in combination with an enhanced content of C, requires a certain amount of β-stabilizing elements, e.g. Mo. In the present study, the solidification pathway, C-solubility and phase evolution of C-containing TNM variants are investigated. Finally, the creep behavior of a refined TNM alloy with 1.5 at.% Mo and 0.5 at.% C is compared with that exhibiting a nominal Ti-43.5Al-4Nb-1Mo-0.1B alloy composition.

1. Introduction

Advanced intermetallic β-solidifying γ-TiAl based alloys, such as TNM alloys with a composition range of Ti-(42-44)Al-(3-5)Nb-(0.1-2)Mo-(0.1-0.2)B (all compositions in at.%, unless stated otherwise), are known as promising candidates to replace heavy Ni-base superalloys as turbine blade materials in aircraft engines as well as turbocharger wheels in automobile combustion engines [1–5]. At room temperature (RT) TNM alloys exist predominantly of γ-TiAl and α_2-Ti_3Al phase as well as minor amounts of β_o-TiAl-phase. Details about the TNM design and alloying concept are published in [5–8]. The increasing demand on light-weight construction, higher efficiency and better performance of air-jet propulsion engines enforce the need and development of more creep-resistant γ-TiAl based alloys to raise the current application limit of about 750 °C [5].

Compared to microstructural aspects, the increase of creep resistance is primarily attributed to the chemical composition of the alloy [4,5,9,10]. It is well established that substitutional elements like Nb, Mo, Ta, and W as well as the interstitial elements C and N show a positive effect on the creep properties of γ-TiAl based alloys [4,5,9–11]. For high Nb- and Mo-containing TiAl alloys, solid solution hardening by Nb and Mo is the dominating hardening effect of the γ-TiAl phase. In addition, alloying of Nb and Mo leads to reduced diffusivity and, thus, to retarded thermal activated dislocation climb during creep [12,13]. The same solid solution hardening effect is attributed to C below its solubility limit [14]. Additionally, cubic perovskite Ti_3AlC

carbides (p-type) can further enhance strength and creep performance due to precipitation hardening as shown for a variety of γ-TiAl-based alloys [4,9,15,16]. Contrarily, the hexagonal Ti_2AlC carbide (h-type), which is thermodynamically stable at higher temperatures, is known to be less efficient to impede dislocation mobility [4,15]. However, it has to be noted that a decrease of dislocation mobility, which corresponds to a higher creep resistance, is always accompanied by a loss of ductility at ambient temperature, which makes the development of high-temperature resistant TiAl alloys with balanced mechanical properties difficult.

For binary γ-TiAl-based alloys, C-solubility in the γ-phase ($L1_0$-structure) is very low because of the presence of Ti_2Al_4- and Ti_4Al_2-type octahedral sites within the $L1_0$-lattice as shown in Fig. 1a [17–19]. The addition of Nb significantly increases the solubility limit of C within the γ-phase due to the formation of antisite defects leading to a certain content of beneficial Ti_6-type octahedral sites [18–20]. Here, Nb occupies Ti-sites within the Ti-sublattice [21] and forces the occupation of Ti in the Al-sublattice of the γ-phase. As a consequence, octahedral sites are formed, which are surrounded only by Ti (Nb) atoms, where C is preferentially dissolved. Generally, C-solubility is increased with a higher Ti/Al ratio [20]. Ti_6-type octahedral sites exist predominantly within the α_2-Ti_3Al phase with $D0_{19}$-structure (Fig. 1b) [18]. The native presence of Ti_6-type sites explains their about 6 times higher C solubility, when compared to the γ-phase [18,20]. An analysis of carbide precipitation and their thermal stability in powder metallurgically produced Nb-rich Ti-45Al-5Nb-(0.5-1)C alloys, so called TNB alloys, can be found in [22,23]. Therein, carbide precipitation was observed at a nominal C-content of 0.75 at.% in the hot-isostatically pressed (HIP) materials condition.

Furthermore, the addition of the solid solution hardening elements such as Nb and Mo leads to a pronounced stabilization of the high-temperature disordered bcc β-Ti(Al)-phase (A2-structure), whereas Mo has an approximately 4 times stronger effect than Nb [24]. It is assumed, however, that the β-phase and its ordered counterpart β_o-TiAl with B2-structure have only a small solubility for C.

Carbon is known to be a strong stabilizer of the hcp α-phase (A3-structure) and increases significantly the eutectoid temperature T_{eut}, which corresponds to the beginning of the disordering reaction $\alpha_2 \rightarrow \alpha$ during heating [12,25]. Its influence on the γ-solvus temperature $T_{\gamma solv}$ was found to be small [25]. Because C is not incorporated in the commercially available TiAl database, its effect on the phase evolution of high Nb- and Mo-containing TiAl-based alloys cannot be predicted by thermodynamic calculations [25–27]. However, the knowledge of the evolution of phase fractions in dependence of the C-content is essential for defining hot-working and heat-treatment parameters of TiAl alloys and can also be used to improve the thermodynamic database.

2. Materials and experimental

The materials used in this investigation were produced by GfE Metalle und Materialien GmbH, Nuremberg, Germany. Details about melting and casting technology are given in [5,28]. Thereby, compacted prematerial within a composition range of Ti-43.5Al-4Nb-(1-1.5)Mo-0.1B-(0-1)C (in at.%) was melted in a vacuum arc furnace for several times (Table 1). Subsequently, the re-melted prematerials were cast via centrifugal casting (CC) or gravity casting (GC) to ingots with 58 mm in diameter. The ingots were HIPed at 1200 °C for 4 hours and 200 MPa followed by furnace cooling. Table 1 summarizes all investigated alloy variants. Additionally, the TNM variants with 0.5 – 1 at.% C were near conventionally hot-forged by Böhler Schmiedetechnik GmbH & Co KG, Austria, via the so-called hot-die process [8,29] and subsequently subjected to a recrystallization annealing at 1175°C near T_{eut} in order to adjust a fine-grained microstructure [30] which is also required to improve statistics for the ensuing X-ray diffraction (XRD) investigations. In addition, a TNM-0.25C alloy variant was produced as button on lab-scale equipment in order to study the phase evolution between the C-free TNM and the TNM-0.5C alloy. The small button was not HIPed, but a heat-treatment with the HIP and recrystallization parameters was conducted in order to provide a similar thermal history.

The macrostructures of the cast and HIPed (cast/HIP) ingot variants were investigated by a stereomicroscope Discovery V20 from Zeiss, Germany, equipped with an AxioCam MRc5 camera. The surface was color-etched with an Ence Margolin solution according to [31]. All microstructures were analyzed subsequent to grinding and electrolytic polishing employing a scanning electron microscope (SEM) Zeiss EVO 50, Germany, with LaB_6-cathode in back-scattered electron (BSE) mode. Energy-dispersive X-ray spectroscopy (EDS) was performed with an INCA Dry Cool from Oxford Instruments, Great Britain, on mechanical polished specimens to prevent carbide dissolution, which is commonly observed in case of electrolytic polishing. Details on metallographic preparation can be found in [31]. Conventional transmission electron microscopy (TEM) was applied using a Philips CM12 operating at 120 kV in order to study carbide formation below the resolution limit of the used X-ray diffraction techniques. Therefore, cut slices with a diameter of 3 mm were ground to a thickness of 100 µm and thinned electrolytically with an A3-electrolyte from Struers, Germany, cooled to -12 °C.

The cast/HIP ingot variants were subjected to texture measurements by means of high-energy X-ray diffraction (HEXRD) at the side station of beamline HEMS, P07B, operated by HZG at Petra III, DESY, Hamburg, Germany. The texture measurements were conducted on cylindrical samples with 10 mm in diameter in transmission geometry with a photon energy of 87 keV (wavelength λ = 0.1425 Å) and beam size

of about 0.8 x 0.8 mm^2. Due to the monochromator optics of the side station the primary beam contains a fraction of the second order of the adjusted wavelength. Whereas, the appearance of upper harmonics has no influence on texture evaluation, it is disadvantageous for phase identification due to the occurrence of additional diffraction peaks. The diffraction patterns were recorded with a Perkin Elmer XRD 1622 flat panel detector suitable for fast measurements. Thereby, the samples were rotated 180° around the vertical cylinder axis in 5° steps for the fine-grained microstructures and in 2° steps for the coarse-grained microstructures [32,33]. The small diffraction angles allow the collection of complete discrete pole figures for all phases simultaneously. The evaluation of raw data in respect to the generation of azimuthal sections of the recorded 2D-diffraction patterns was done by the software Fit2D [34,35]. Subsequently, the resulting chi-files obtained from Fit2D were converted to esg-files for further texture evaluation with the program MAUD [36]. The orientation distribution functions (ODF) were refined by means of E-WIMV approach [37]. The ODF resolution was defined to be equivalent to the step size of data collection, i.e. 5° or 2°.

HEXRD phase identification experiments for the analysis of carbides at RT were performed in the main station of HZG beamline HEMS, P07-EH3, with a photon energy of 100 keV (λ = 0.124 Å) in order to exploit the high flux of Petra III. Again, a beam cross section of 0.8 x 0.8 mm^2 and a Perkin Elmer XRD 1622 flat panel detector were used.

In situ HEXRD phase evolution experiments were carried out at HZG beamline HARWI II, W2 beamline at Doris III, DESY, using a modified quenching and deformation dilatometer from Bähr Thermoanalyse GmbH, Germany, in combination with a mar555 flat panel detector. A photon energy of 100 keV (λ = 0.124 Å) and a beam size of 1 x 1 mm^2 were applied to achieve good grain statistics. The cast/HIP samples with a size of 5 mm in diameter and 10 mm in length were heated up to 1100 °C and held for 10 min. Subsequently, the samples were heated with a slower heating rate of 2 K/min to 1300 °C. Due to accelerated phase transformation kinetics above 1300 °C a faster heating rate of 15 K/min was applied from 1300 °C to 1425 °C to retard excessive grain growth of the α-phase to minimize the risk of thermocouple tear-off. The temperature was controlled by type B thermocouples, which were spot welded on a Ta-platelet working as diffusion barrier to the sample surface. The phase fractions were evaluated by Rietveld analysis on azimuthally integrated diffraction patterns with the software TOPAS from Bruker-AXS, USA [38–40].

The phase fractions as derived from *in situ* HEXRD measurements were verified for each alloy variant by means of 1 hour heat treatments within the characteristic phase field regions, followed by oil quenching. Therefore, lab-scale XRD measurements with a D8 Advance from Bruker AXS conducted on heat-treated specimens below $T_{\gamma sol v}$ were used to compensate temperature uncertainties of the dilatometer experiments

as described in [39]. The heat treatments were performed in a high-temperature furnace RHF 16/15 of Carbolite, Great Britain, on specimens with a size of about 1 x 1 x 1 cm^3. The temperature was controlled by thermocouples of type S.

Differential scanning calorimetry (DSC) was conducted with a Setsys Evolution of Setaram, France, for the verification of the solidification pathways in the temperature range from 1350 to 1550 °C. Samples with a mass of 20 mg were heated up in an Al_2O_3 crucible under Ar-atmosphere using a gas flow of 50 ml/min. The phase transition temperatures were extrapolated to 0 K/min from 4 different heating rates (6, 15, 23, and 40 K/min) in order to obtain thermodynamic equilibrium values. Additionally, each heating rate was calibrated by enthalpy standards [25].

Hardness measurements corresponding to Vickers HV10 were performed on electrolytic polished specimens using a universal hardness testing machine M4C 025 G3M from Emco-Test, Austria. The arithmetic mean value was derived from 5 individual hardness measurements.

Creep tests were carried out for 300 hours under constant loading of 150 MPa at 780 °C with a Mark II TC 30 creep testing machine from Denison Mayes Group, Great Britain. The gauge volume of the specimens corresponds to 30 mm in length and 6 mm in diameter. The experimentally derived creep curves were fitted with a function based on the Garofalo equation [41] to achieve higher accuracy in the determination of the minimal creep rate. The creep curve fitting was applied with the software Origin 8.5.1 from OriginLab Corporation, USA.

3. Results and discussion

3.1 Structural and textural evolution

The cast/HIP macrostructures of the ingot variants TNM and TNM-(0.5-1)C are shown in Fig. 2a. Here, the C-free TNM alloy shows a homogeneous and fine-grained macrostructure within the entire cross section due to solidification via the β-phase (the exact positions, where the metallographic specimens were taken from the ingot, are indicated in Fig. 2b). An increase of 0.5 at.% C leads to a significant change of the macrostructure. Whereas the circumferential area appears fine-grained, the major part of the cross-section exists of coarse columnar α_2/γ-colonies aligned in radial direction (RD) according to the temperature gradient present during solidification of the ingot. This structural difference indicates a change in solidification behavior, i.e. from β- to peritectic solidification. For the TNM-0.75C alloy the fine-grained zone is smaller than that of the 0.5 at.% C variant. It is tempting to speculate that grains from the fine-grained zone act as nucleation sites according to the Burgers orientation relationship $\{110\}_\beta \parallel (0001)_\alpha$ and $\langle 111\rangle_\beta \parallel \langle 11\bar{2}0\rangle_\alpha$ [42]

and trigger the formation and growth of the columnar α-grains in the direction of heat extraction. The columnar α-grains are present as α_2/γ-colonies at RT [43,44]. Therefore, $\langle 0001 \rangle_{\alpha 2}$ and $\langle 111 \rangle_{\gamma}$ are parallel to RD [44] according to the Blackburn orientation relationship $(0001)_{\alpha 2} \parallel \{111\}_{\gamma}$ and $\langle 11\bar{2}0 \rangle_{\alpha 2} \parallel \langle 101]_{\gamma}$ [45]. For the TNM-1C alloying variant, again a fine-grained solidification structure exists, whereas the grains seem to be coarser when compared to the C-free TNM alloy.

The corresponding microstructures of Fig. 2 are shown in Fig. 3. Thereby, the TNM alloy in Fig. 3a exhibits the highest content of β_o-phase at RT. For the alloy variants with 0.5 and 0.75 at.% C, Al-rich segregations arise due to the peritectic solidification reaction [46] which obviously cannot be compensated by subsequent HIPing (Figs. 3b,c). Furthermore, the presence of residual dendrites with β-stabilizing elements points to a peritectic solidification pathway primary via the β-phase according to $L \rightarrow L+\beta \rightarrow \alpha\ (+\beta)$ [46]. The grain refinement of the TNM-1C alloy is attributed to the formation of an additional phase, i.e. carbide formation (Fig. 3d). SEM-EDS indicates this phase as h-type carbide $(Ti,Nb)_2AlC$ as derived from the measured chemical composition of Ti-23.5Al-2.5Nb-31.0C, where the Ti-content is about a factor of 2 higher than the Al-content. Nb tends to be dissolved within the Ti-sublattice [21]. The detection inaccuracy for C is about ± 5 at.%, therefore, the obtained chemical composition of the h-type carbide can only be seen as a first qualitative trend.

The results of texture measurements conducted on specimens in the cast/HIP condition are shown in Fig. 4. The recalculated $(0001)\alpha_2$ pole figure (PF) of the TNM alloy shown in Fig. 4a gives no indication for the presence of a statistically significant texture as already expected from the macro- and micrographs. This result is in agreement with texture measurements, where neutrons have been used [47]. In contrast, for the TNM-0.5C alloy, also representing the TNM-0.75C alloying variant, a sharp solidification texture is observed (see Figs. 4b,c). The recalculated $(0001)\alpha_2$ PF in Fig. 4b shows two sharp orientation density spots in RD, according to columnar α_2/γ-colonies perpendicular to the normal direction (ND). ND is parallel to the ingot axis (see Fig. 2b). The weaker spots of the TNM-0.5C $(0001)\alpha_2$ PF are propably formed during HIPing. In Fig. 4c, the recalculated $\{11\bar{2}0\}\alpha_2$ PF confirms the rotation-symmetric orientation of the columnar α_2/γ-colonies around RD according to [43,44]. In the TNM-1C alloy, h-type carbides act as efficient grain refiners and lead to a nearly texture-free microstructure again (Fig. 4d).

For the identification of additional phases and the evaluation of phase fractions by HEXRD experiments, the microstructures of the cast/HIP TNM-0.5C and TNM-0.75C alloys are not suitable due to their strong solidification textures, i.e. insufficient grain statistics and accordingly phases are not visible when they are not in diffraction condition. In order to overcome these shortcomings, the ingot variants of the C-containing

alloys were forged and subsequent heat-treated to obtain a fine-grained microstructure with better grain statistics (Fig. 5). To rule out textural effects by azimuthal integration, the forging direction of the specimens was oriented parallel to the detector plane [48]. In case of TNM-0.5C the coarse α_2/γ-colonies could not be completely recrystallized even at a local deformation of $\varphi \approx -0.9$ (Fig. 5a), but the amount of fine-grained zones is significantly higher when compared to the cast/HIP TNM-0.5C microstructure (Fig. 3b). Because of the α-stabilizing effect of C, the amount of β_o-phase in TNM-0.75C is reduced and coarse-grained α_2/γ-colonies are still remaining within the microstructure (Fig. 5b). After deformation and heat-treatment of the fine-grained TNM-1C material, the microstructure mainly consists of recrystallized α_2- and γ-grains as well as aligned h-type carbides (Fig. 5c). Obviously, within all investigated TNM-(0.5-1)C alloys a significant fraction of undesired deformation-induced micropores are present, which might be the result of an unfavorable high C-content and/or the low temperature at the end of the hot-die forging process.

High resolution HEXRD phase identification experiments confirm the presence of h-type Ti_2AlC carbides in the TNM-1C alloy (see Fig. 6). For the h-type carbide the lattice parameters are calculated from the peak positions to c = 13.70 Å and a = 3.05 Å. Contrarily, for the alloying variants TNM-0.5C and TNM-0.75C no indications for the presence of carbides were found. For all TNM-(0.5-1)C alloys additional peaks can be attributed to the orthorhombic TiB-phase with B27-structure (see Fig. 6). The experimentally determined lattice parameters are a = 6.13 Å, b = 3.06 Å and c = 4.59 Å.

3.2 Carbon solubility and carbide formation

The appearing phase fractions of the forged and heat-treated microstructures at RT prove the α-stabilizing effect of carbon (Fig. 7a). While the fraction of the γ-phase remains nearly constant with increasing content of C, the amount of α_2-phase increases by a factor of about 2.5, from 15 m.% for the TNM alloy to 40 m.% for the TNM-(0.5-1)C alloys. Accordingly, the fraction of β_o-phase is reduced from 23 m.% to smaller than 5 m.% for TNM-0.5C and TNM-0.75C until it seems to vanish for TNM-1C, i.e. phase fraction of β_o is below the resolution limit, which is in good agreement with the micrographs shown in Fig. 5.

The change of the unit cell volume of the major constituting phases γ, α_2 and β_o in dependence on the C-content is shown in Fig. 7b. As a reference, the unit cell volumes of the forged and heat-treated TNM alloy were determined to be 133.2 $Å^3$ for α_2, 33.1 $Å^3$ for β_o and 65.6 $Å^3$ for γ [49,50]. The β_o-phase does not show a trend in the change of unit cell volume, accordingly no significant amount of C is dissolved within the β_o-phase. α_2- and γ-phase, however, show a pronounced increase of their unit cell volume. Both phases reach a plateau, when the C-solubility limit is exceeded and carbide formation takes place. In case of TNM-1C the

C-solubility is enhanced due to a higher Ti/Al ratio when compared to TNM-0.75C (see Table 1). From SEM and high-resolution HEXRD investigations no indication for the formation of carbides within the TNM-0.75C alloy was found, which is not in agreement with powder-metallurgically produced TNB alloys, where p-type carbides are already present for 0.75 at.% C [23]. However, these alloys differ in Al and Nb concentrations. TEM investigations confirm the absence of h- and p-type carbides within the cast/HIP as well as forged and heat-treated TNM-0.75C material (see Fig. 8). No indication of carbide formation was found within the γ- and β_o- phase, which have a lower C-solubility when compared to the α_2-phase. Also no carbide precipitates were found at β_o/γ- or γ/γ-interfaces. The higher C-solubility within the studied TNM system in comparison to the TNB alloy in [23] can be attributed to a higher Ti/Al ratio as well as a higher α_2-phase fraction by a factor of 2. In the present study, h-type carbides were found only in the TNM-1C alloy, but no p-type carbides were detected. Therefore, the overall carbon solubility limit of TNM alloys is between 0.75 and 1 at.% C. Assuming, that the overall C-solubility limit is 0.75 at.% and the C-solubility limit of the α_2-phase is about 6 times higher than in the γ-phase [20] with about 40 at.% α_2- and 60 at.% γ-phase present (see Fig. 7a), the maximum C-solubility can be estimated to be 1.5 at.% in the α_2-phase and 0.25 at.% in the γ-phase. In this estimation, a C-content dissolved at interfaces was neglected. In a forthcoming study, atom probe analysis will be conducted to determine the maximum C-solubility of α_2-, γ- and β_o-phase.

The evolution of hardness with C-content of forged and heat-treated material is shown in Fig. 7c. The hardness increases about 100 HV10 until the C-solubility limit is reached corresponding to a gain in hardness of + 25 %. Above the C-solubility limit, precipitation of coarse h-type carbides does not further improve hardness. The appearance of a hardness plateau suggests further the absence of fine p-type carbides when compared to the HIPed C-doped TNB alloys in [23]. Thus, solid solution hardening is proposed to be the major contributing strengthening effect in the investigated forged and heat-treated TNM-C alloys. It has to be mentioned that the heat-treated TNM-0.25C button shows a good agreement with regard to phase fractions and unit cell volumes when compared to the forged and heat-treated ingot variants (Figs. 7a,b), but cannot accurately reproduce the trend for hardness (Fig. 7c). This can be explained by the missing HIPing and forging step which in turn lead to a different microstructure.

3.3 Experimental phase diagram

The experimentally determined phase diagram of the TNM-(0-1)C system is shown in Fig. 9. The solidification sequence was studied by means of DSC measurements as described in section 2 and comprehensively reported in [25,51]. The C-free TNM alloy solidifies via the β-phase according to the

pathway L → L+β → β → β+α → … . For simplicity the role of Ti-borides as efficient grain refiners is not included in the sequence [5,52]. TNM alloys which solidify completely via the β-phase show a β → α phase transformation exhibiting the Burgers orientation relationship stated in section 3.1. According to this, within a single β-grain α-grains with up to 12 orientation variants can be formed, leading to an intrinsic grain refinement which is not possible in case of a peritectic solidification. With increasing content of C the solidification pathway changes from β- to peritectic solidification as observed for the TNM-(0.5-1)C alloys. Thus, the solidification pathway changes to L → L+β → L+β+α → β+α → … (see phase diagram in Fig. 9). For the TNM-0.5C and TNM-0.75C alloys peritectic solidification leads to a coarse-grained columnar microstructure with sharp solidification texture (see Fig. 2) as reported also for other peritectically solidifying γ-TiAl based alloys [46,53]. The grain refining effect within the TNM-1C alloy is attributed to the formation of h-type carbides and, thus, to an enhancement of heterogeneous nucleation during the subsequent solid-state phase transformations.

The phase fraction diagrams and the phase transition temperatures of the different alloys were derived by means of *in situ* HEXRD heating experiments (see Fig. 10). With increasing C-concentration the β-phase fraction in the vicinity of $T_{\gamma solv}$ decreases significantly, leading to an increase of α-phase. In addition to the C-free TNM alloy complete solidification via the β-phase can also be observed for the TNM-0.25C alloy, because of the appearance of a single β-phase field region. The circle denoted as 1 in Fig. 9, indicates where the solidification pathway changes from β- to peritectic solidification. According to the quasi-binary Ti-Al-4Nb-1Mo-0.1B section reported in [54,55], C has an about 6 times stronger effect on α-stabilization than Al, i.e. about 2.7 at.% Al have to be added to a TNM alloy with an Al-content of 43.2 at.% to cause peritectic solidification. The same effect results from the addition of about 0.45 at.% C to a C-free TNM alloy. For the TNM-(0.5-1)C alloys no occurrence of a single β-phase field region was found, which agrees well with the change in solidification behavior measured by DSC experiments. The decrease of β-phase also leads to the formation of a pronounced single α-phase field region, which is about 50 °C wide for the TNM-0.25C alloy and increases to about 150 °C for the TNM-1C alloy. Circle 2 in Fig. 9 marks the beginning of the formation of a single α-phase field region with increasing C-content. The starting point was estimated taking into account a 6 times higher α-stabilizing effect of C when compared to that of Al. $T_{\gamma solv}$, which indicates the lower boundary of the single α-phase field region, is almost independent from the C-content as reported also in [25] for C-containing TNB alloys. The variation of $T_{\gamma solv}$ is primarily assigned to the different Al-contents of the investigated alloys (see Table 1) [24]. In contrast, addition of C strongly affects the $\alpha_2 \rightarrow \alpha$ disordering temperature T_{eut}. For TNM-1C an increase of about 75 °C was observed when compared to the C-free TNM

alloy. Accordingly, Chladil *et al.* [25] reported an increase of T_{eut} of about 50 °C for Ti-45Al-(5-7.5)Nb-0.5C alloys. Between 0.75 and 1 at.% C the disordering reaction even proceeds within the (α+γ)-phase field region (see circle 3 in Fig. 9). In contrast, the low content of β_o/β-phase and the weak superstructure peaks of the β_o-phase in XRD-patterns [39] did not allow an accurate determination of the $\beta_o \rightarrow \beta$ disordering reaction for the different alloy compositions. Finally, for the TNM-1C alloy an *in situ* HEXRD experiment with a heating rate of 2 K/min was conducted to study the temperature stability of the h-type Ti_2AlC carbide. The dissolution temperature T_{hsolv} was determined to be 1410°C, which agrees well with the investigations conducted on a TNB alloy as reported in [22]. Therefore, h-type carbides are supposed to have a grain refining effect during the solid-state phase transformations which occur during cooling. Complementary to the *in situ* HEXRD phase evolution experiments, static heat treatments were applied to verify the occurring phase field regions. Representative micrographs are summarized in Fig. 11 and match well with the results derived from HEXRD investigations. It has to be noted, that after oil quenching to RT a single β-phase field region of the TNM alloy at 1400 °C appears as two-phase (α_2+β_o)-microstructure due to the fast re-transformation kinetics $\beta \rightarrow \alpha$ [24,55]. As a consequence, the high-temperature phase fractions present in TNM specimens cannot accurately be determined when metallographic specimens are annealed at $T > T_{\gamma solv}$ and subsequently oil quenched [56]. For peritectic TNM-(0.5-1)C alloys the grain refining effect by the $\beta \rightarrow \alpha$ phase transformation is not efficient anymore due to minor amounts of β-phase within the (α+β)-phase field region, i.e. the disappearance of the single β-phase field region leads to an inhomogeneous refinement of the former β-phase during oil quenching. The segregation existing in all peritectic solidified alloys could not be compensated during the 1 hour heat treatments at $T < T_{\gamma solv}$. Furthermore, for TNM-0.75C after annealing at 1250 °C and 1350 °C a certain amount of β_o-phase is present, which can arise due to segregational effects and/or temperature uncertainties during heat treatments near phase field boundaries (see Fig. 9).

3.4 Refined alloy composition

Maintaining β-solidification combined with an increased content of dissolved C, e.g. 0.5 at.%, makes it necessary to reverse the solidification pathway from peritectic to β-solidification by alloying higher amounts of β-stabilizing elements such as Nb or Mo. In the present study, the β-stabilizing effect is obtained by increasing the Mo-concentration from 1 to 1.5 at.% (Table 1). The microstructure of the refined TN1.5Mo-0.5C alloy is displayed in Fig. 12a. The cast/HIP microstructure exhibits a hardness of ~ 380 HV10, which is about 30 HV10 higher than the hardness of the C-free TNM alloy in the same condition. The TN1.5Mo-0.5C alloy consists of 24 m.% α_2-, 11 m.% β_o-, and 65 m.% γ-phase, whereas the TNM alloy is composed of

22 m.% α_2-, 15 m.% β_o-, and 63 m.% γ-phase. Thus, phase fractions and morphological appearance of the microstructures are nearly the same and the differences in hardness can be primarily attributed to additional solid solution hardening caused by Mo and C. Such as the TNM alloy, the fine-grained TN1.5Mo-0.5C alloy exhibits no statistical significant texture in the cast/HIP condition as proved by the recalculated (0001)α_2 pole figure shown in Fig. 12b.

The phase fraction diagram obtained by *in situ* HEXRD for the TN1.5Mo-0.5C alloy depicts the typical C-shaped course of the β-phase without the occurrence of a single α-phase field region. The evolution of phase fractions resembles that of the TNM alloy (Fig. 10), however, the β-transus temperature T_β is shifted to a higher temperature. For the TNM alloy T_β was determined to be 1380 °C (Fig. 9), whereas the single β-phase field could not be reached even at 1450 °C in case of the TN1.5Mo-0.5C alloy.

The refined solid solution hardened TN1.5Mo-0.5C alloy variant shows an improved creep performance when compared to the TNM alloy (Fig. 13). After short-term creep tests at 780 °C and 150 MPa for 310 hours the creep strain of the TN1.5Mo-0.5C alloy is more than 50 % smaller than that obtained for the C-free TNM alloy (Fig. 13a). From Fig. 13b it is evident that the TN1.5Mo-0.5C alloy has not reached the minimum creep rate $\dot{\varepsilon}_{min}$, whereas the TNM alloy has already passed $\dot{\varepsilon}_{min}$. The minimum creep rate is $2.4 \cdot 10^{-8}$ s^{-1} for the TNM alloy and decreases to about $8.4 \cdot 10^{-9}$ s^{-1} for the TN1.5Mo-0.5C alloy. HEXRD and TEM investigations carried out on crept specimens have found evidence of creep-induced precipitation of p-type Ti_3AlC carbides. Rietveld analysis after creep testing at RT shows a change of the phase fractions to 18.5 m.%, 12 m.%, 68 m.% and 1.5 m.% for α_2, β_o, γ, and Ti_3AlC, respectively. No significant difference between the gauge volume and the unstressed gripping head of the crept specimens was detected. Therein, the amount of α_2-phase decreases at the expense of γ-phase, while the content of β_o-phase remains constant. Additionally, p-type Ti_3AlC carbides were formed. Therefore, the change of the phase contents is primarily attributed to the thermodynamic disequilibrium of the cast/HIP starting microstructure. Furthermore, no ω-phase was detected in the C-containing TN1.5Mo-0.5C alloy variant when compared to the C-free TNM alloy [8]. The TEM images within the gauge volume of the TN1.5Mo-0.5C alloy are shown in Fig. 14 and indicate location and morphology of p-type carbide precipitation. The arrow in Fig. 14a marks deformation-induced p-type carbides nucleated at dislocations. These features are not present in the stress-free gripping head of the crept sample. However, the major content of p-type carbides was formed within the γ-phase of the α_2/γ-colonies due to the excess of C resulting from the decreasing α_2-phase fraction and the reduced C-solubility of the γ-phase at testing conditions (Fig. 14b). Thereby, this coarse p-type carbides nucleate at α_2/γ-interfaces and grow into the γ-phase according to the orientation relationship $(001)_\gamma \parallel (001)_p$ and

$(010)_\gamma$ || $(010)_p$ as proposed by Tian *et al.* [15]. From the HEXRD investigations of the crept specimens the lattice parameter of the p-type carbide Ti_3AlC was determined to a = 4.155 Å. The lattice mismatch and the resulting stress field leads to a growth of elongated p-type carbides in the [001]-direction of the γ-phase as reported in [16]. Hardness tests within the gauge volume and the head of the crept specimens reveal that the phase fraction evolution during creep testing does not affect the hardness when compared to the cast/HIP starting condition. Thus, the formation of coarse p-type carbides within the α_2/γ-colonies and the precipitation of smaller p-type carbides at dislocations seem not to contribute significantly to an increase of hardness. It also has to be mentioned that the raising content of γ-phase and the observed alteration of the lamellar structure have an opposite effect on hardness.

4. Conclusions

Based on the alloying concept developed for β-solidifying TNM alloys, the influence of C on solidification pathway, phase evolution and microstructure was studied. With increasing C-concentration, i.e. at 0.45 at.%, the solidification behavior changes from solidification via the β-phase to peritectic solidification, which leads to a coarse-grained columnar microstructure exhibiting a sharp solidification texture. Crossing the solubility limit of C, which is below 1 at.% C for the alloys investigated, leads to the precipitation of h-type carbides Ti_2AlC and to a refinement of the α_2/γ-colony structure, probably due to enhanced heterogeneous nucleation during the ensuing solid-state phase transformations. From a simple estimation a maximum C-solubility of about 1.5 at.% was calculated for the α_2-phase and about 0.25 at.% for the γ-phase. The precipitation of perovskite-type Ti_3AlC carbides was not observed for the investigated materials conditions. Carbon increases the $\alpha_2 \rightarrow \alpha$ disordering temperature T_{eut} of TNM-based alloys and acts as an about 6 times stronger α-stabilizer than Al. The α-stabilization leads to the formation of a pronounced single α-phase field region, which widens with increasing C-content. $T_{\gamma solv}$ was found to be nearly unaffected from C and its change is primarily connected to fluctuations of the Al-content. The preservation of β-solidification, i.e. to exhibit a fine-grained and almost texture-free microstructure in combination with a high concentration of dissolved C, requires a further increase of β-stabilizing elements, i.e. Mo. Alloying with C and Mo was found to be an efficient alloying strategy to improve the creep performance of TNM-based alloys due to solid solution hardening as well as the precipitation of creep-induced p-type Ti_3AlC carbides.

Acknowledgement

The present study was conducted within the framework of the German BMBF project O3X3530A. The support of the DESY management, User Office and HZG beamline staff for performing *in situ* HEXRD experiments at HARWI II, W2 beamline, and HEXRD measurements at HEMS, P07 and P07B beamline, is gratefully acknowledged. In particular, the authors thank Dr. Thomas Lippmann and Dr. Norbert Schell for their assistance at the beamlines. The research activities also received funding from the European Community's 7^{th} Framework Programme (FP7/2007e2013) under grant agreement no. 226716.

References

[1] Appel F, Oehring M. γ-Titanium Aluminide Alloys: Alloy Design and Properties, in: Titanium and Titanium Alloys. Weinheim: WILEY-VCH; 2003.

[2] Kestler H, Clemens H. Production, Processing and Applications of γ-TiAl Based Alloys, in: Titanium and Titanium Alloys: Fundamentals and Applications. Weinheim: WILEY-VCH; 2003.

[3] Kim YW, Morris D, Yang R, Leyens C. Structural Aluminides for Elevated Temperature Applications. Warrendale: TMS; 2008.

[4] Appel F, Paul JDH, Oehring M. Gamma titanium aluminide alloys: science and technology. Weinheim: Wiley-VCH; 2011.

[5] Clemens H, Mayer S. Advanced Engineering Materials 2013;15:191.

[6] Chladil H, Clemens H, Otto A, Güther V, Kremmer S, Bartels A, Gerling R. BHM 2006;151:356.

[7] Clemens H, Wallgram W, Kremmer S, Güther V, Otto A, Bartels A. Advanced Engineering Materials 2008;10:707.

[8] Wallgram W, Schmoelzer T, Cha L, Das G, Güther V, Clemens H. International Journal of Materials Research 2009;100:1021.

[9] Appel F, Oehring M, Wagner R. Intermetallics 2000;8:1283.

[10] Imayev RM, Imayev VM, Khismatullin TG, Oehring M, Appel F. The Physics of Metals and Metallography 2006;102:105.

[11] Kawabata T, Tadano M, Izumi O. ISIJ International 1991;31:1161.

[12] Park HS, Nam SW, Kim NJ, Hwang SK. Scripta Materialia 1999;41:1197.

[13] Appel F, Paul JDH, Oehring M, Fröbel U, Lorenz U. Metallurgical and Materials Transactions A: Physical Metallurgy and Materials Science 2003;34 A:2149.

[14] Appel F, Lorenz U, Oehring M, Sparka U, Wagner R. Materials Science and Engineering: A 1997;233:1.

[15] Tian WH, Nemoto M. Intermetallics 1997;5:237.

[16] Christoph U, Appel F, Wagner R. Materials Science and Engineering A 1997;239-240:39.

[17] Denquin A, Naka S, Huguet A, Menand A. Scripta Metallurgica et Materialia 1993;28:1131.

[18] Menand A, Huguet A, Nérac-Partaix A. Acta Materialia 1996;44:4729.

[19] Menand A, Zapolsky-Tatarenko H, Nérac-Partaix A. Materials Science and Engineering: A 1998;250:55.

[20] Scheu C, Stergar E, Schober M, Cha L, Clemens H, Bartels A, Schimansky F-P, Cerezo A. Acta Materialia 2009;57:1504.

[21] Song Y, Yang R, Li D, Hu ZQ, Guo ZX. Intermetallics 2000;8:563.

[22] Stark A, Oehring M, Pyczak F, Schell N, Schreyer A. Carbide Formation in Nb-rich Gamma Titanium Aluminides, in: HASYLAB Annual Report. Hamburg: HASYLAB/DESY; 2011.

[23] Gabrisch H, Stark A, Schimansky F-P, Wang L, Schell N, Lorenz U, Pyczak F. Intermetallics 2013;33:44.

[24] Schloffer M, Themessl A, Schwaighofer E, Clemens H, Heutling F, Helm D, Achtermann M, Mayer S. Phase Transitions and Phase Equilibria in the TiAl-Nb-Mo System, in: Presentation at 4th International Workshop on Titanium Aluminides. Nuremberg, Germany: GfE Metalle Und Materialien GmbH; 2011.

[25] Chladil HF, Clemens H, Leitner H, Bartels A, Gerling R, Schimansky FP, Kremmer S. Intermetallics 2006;14:1194.

[26] Saunders N. Phase Equilibria in Multi-component γ-TiAl Based Alloys, in: Kim YW, Dimiduk DM, Loretto MH (Eds.). Gamma Titanium Aluminides. Warrendale, PA: TMS; 1999.

[27] Schwaighofer E, Clemens H, Mayer S. unpublished data 2009 – 2012.

[28] Achtermann M, Fürwitt W, Guether V, Nicolai H-P. Patent EP2010/064306, 2011.

[29] Kremmer S, Chladil H, Clemens H, Otto A, Güther V. Near Conventional Forging of Titanium Aluminides, in: Ti-2007 Science and Technology, vol. 2. Sendai, Japan: The Japan Institute of Metals (JIM); 2008.

[30] Wallgram W, Clemens H, Schloffer M. Patent application number 20110277891, 2011.

[31] Schloffer M, Schmoelzer T, Mayer S, Schwaighofer E, Hawranek G, Schimansky FP, Pyczak F, Clemens H. Practical metallography 2011;48:594.

[32] Lonardelli I, Wenk H-R, Lutterotti L, Goodwin M. Journal of Synchrotron Radiation 2005;12:354.

[33] Carradò A, Brokmeier H-G, Pirling T, Wimpory RC, Schell N, Palkowski H. Advanced Engineering Materials 2013:in press. DOI 10.1002/adem.201200161.

[34] Hammersley AP, Svensson SO, Hanfland M, Fitch AN, Häusermann D. High Pressure Research 1996;14:235.

[35] Merkel S. The Radial Diffraction Files, accessed 11 Mar. 2013. URL: http://merkel.zoneo.net/RDX/index.php.

[36] Lutterotti L, Bortolotti M, Ischia G, Lonardelli I, Wenk H-R. Zeitschrift für Kristallographie Supplements 2007;26:125.

[37] Chateigner D. Combined Analysis. London, UK□ : Hoboken, NJ: ISTE□ ; Wiley; 2010.

[38] McCusker LB, Von Dreele RB, Cox DE, Louër D, Scardi P. Journal of Applied Crystallography 1999;32:36.

[39] Schmoelzer T, Liss K-D, Zickler GA, Watson IJ, Droessler LM, Wallgram W, Buslaps T, Studer A, Clemens H. Intermetallics 2010;18:1544.

[40] Schmoelzer T, Liss K-D, Staron P, Mayer S, Clemens H. Advanced Engineering Materials 2011;13:685.

[41] Garofalo F. Resistance to Creep Deformation and Fracture in Metals and Alloys, in: Committee E08 (Ed.). Properties of Crystalline Solids. West Conshohocken, PA: ASTM International; 1961.

[42] Burgers WG. Physica 1934;1:561.

[43] Johnson DR, Inui H, Yamaguchi M. Acta Materialia 1996;44:2523.

[44] Kim SE, Lee YT, Oh MH, Inui H, Yamaguchi M. Materials Science and Engineering: A 2002;329-331:25.

[45] Blackburn MJ. The Science, Technology and Application of Titanium. Oxford: Pergamon Press Ltd.; 1970.

[46] Küstner V. Untersuchungen Zur Gefügebildung Bei Der Erstarrung von γ-Titanaluminid-Legierungen Unterschiedlicher Konstitution. PhD thesis. Technische Fakultät der Christian-Albrechts-Universität zu Kiel, 2003.

[47] Clemens H, Chladil HF, Wallgram W, Zickler GA, Gerling R, Liss KD, Kremmer S, Güther V, Smarsly W. Intermetallics 2008;16:827.

[48] Stark A, Schwaighofer E, Mayer S, Clemens H, Lippmann T, Lottermoser L, Schreyer A, Pyczak F. MRS Proceedings 2013;1516:DOI 10.1557/opl.2012.1577.

[49] Clemens H, Schloffer M, Schwaighofer E, Werner R, Gaitzenauer A, Rashkova B, Schmoelzer T, Pippan R, Mayer S. MRS Proceedings 2013;1516:DOI 10.1557/opl.2012.1654.

[50] Gaitzenauer A, Stark A, Gosslar D, Clemens H, Mayer S. 2013:submitted to Advanced Engineering Materials.

[51] Schwaighofer E. Influence of Heat Treatments on the Microstructure and Mechanical Properties of Cast and Hot-isostatically Pressed TNM Alloys. Diploma thesis. Montanuniversität Leoben, 2010.

[52] Hecht U, Witusiewicz V, Drevermann A, Zollinger J. Intermetallics 2008;16:969.

[53] Küstner V, Oehring M, Chatterjee A, Güther V, Brokmeier H-G, Clemens H, Appel F. An Investigation of Microstructure Formation During Solidification of Gamma Titanium Aluminide Alloys, in: Kim Y-W, Clemens H, Rosenberger AH (Eds.). Gamma Titanium Aluminides 2003. Warrendale: The Minerals, Metals & Materials Society; 2003.

[54] Clemens H, Boeck B, Wallgram W, Schmoelzer T, Droessler LM, Zickler GA, Leitner H, Otto A. Experimental Studies and Thermodynamic Simulations of Phase Transformations in Ti-(41-45)Al-4Nb-1Mo-0.1B Alloys, in: Materials Res. Soc. Symp. Proc., vol. 1128. Warrendale: MRS; 2008.

[55] Schwaighofer E, Clemens H, Mayer S, Lindemann J, Klose J, Smarsly W, Güther V. 2013:submitted to Intermetallics.

[56] Schloffer M, Iqbal F, Gabrisch H, Schwaighofer E, Schimansky FP, Mayer S, Stark A, Lippmann T, Göken M, Pyczak F, Clemens H. Intermetallics 2012;22:231.

Figure captions

Fig. 1: Crystal structures (unit cells are indicated as black lines) and octahedral sites (white lines) of a) γ-TiAl and b) α_2-Ti_3Al phase according to [18]. Carbon is preferentially dissolved within Ti_6-type octahedral sites as shown for α_2-Ti_3Al. In γ-TiAl only Ti_2Al_4- and Ti_4Al_2-type octahedral sites are existing. Alloying with Nb leads to the formation of Ti_6-type octahedral sites within the $L1_0$-structure. Consequently, the C-solubility of the γ-TiAl phase is increased as reported in [18,20].

Fig. 2: a) Macrographs of the cast/HIP ingot variants TNM and TNM-(0.5-1)C; b) position of specimens taken for the macrographs shown in a). In addition the growth direction of the columnar grains are indicated according to [44]. The fine-grained zone, which exists on the circumferential area of the ingot, is not shown in this schematic drawing. ND = Normal direction, RD = radial direction, TD = tangential direction

Fig. 3: SEM micrographs taken in BSE mode of the cast/HIP microstructures corresponding to Fig. 1: a) TNM, b) TNM-0.5C, c) TNM-0.75C, and d) TNM-1C.

Fig. 4: Recalculated pole figures in equal-area projection of a) TNM (0001)α_2, b) TNM-0.5C (0001)α_2, c) TNM-0.5C $\{11\bar{2}0\}\alpha_2$, and d) TNM-1C (0001)α_2. ND is parallel to the ingot axis (see also Fig. 1b).

Fig. 5: Micrographs of forged and heat-treated alloy variants: a) TNM-0.5C, b) TNM-0.75C and c) TNM-1C. Local degree of deformation $\varphi \approx -0.9$. Forging direction is vertical. SEM images taken in BSE mode.

Fig. 6: Azimuthally integrated HEXRD diffraction patterns of forged and heat-treated TNM-(0.5-1)C alloys. The corresponding microstructures are shown in Fig. 5. The additional phase in the TNM-1C alloy corresponds to Ti_2AlC h-type carbide (see arrows).

Fig. 7: Influence of C-addition on a) phase fractions, b) unit cell volume of α_2-, β_o-, γ-phase and c) macro-hardness. Forged and heat-treated materials condition except for TNM-0.25C (see text); RT data.

Fig. 8: TEM bright-field images of TNM-0.75C: a) cast/HIP and b) forged and heat-treated material. For both material conditions no indication for the presence of carbides within the β_o- and γ-phase as well as at β_o/γ- and γ/γ-interfaces were found.

Fig. 9: Experimental phase diagram of the Ti-43.5Al-4Nb-1Mo-0.1B-C alloy system as determined by DSC and *in situ* HEXRD experiments (●) in combination with static heat treatments and subsequent quantitative metallography (see text).

Fig. 10: Phase fraction diagrams of the different TNM-C alloy variants (Table 1) as determined by *in situ* HEXRD experiments.

Fig. 11: SEM micrographs of heat-treated cast/HIP material for the verification of phase field regions. All samples were annealed for 1 hour at the indicated temperature followed by oil quenching to RT. The phase field regions where the heat treatment took place are indicated too. It should be noted that oil quenching from above $T > T_{\gamma sol/}$ does not preserve the original high-temperature microstructure (see text). All SEM images are taken in BSE mode.

Fig. 12: a) SEM-micrograph of β-solidifying TN1.5Mo-0.5C alloy (TNM alloy with 1.5 at.% Mo and 0.5 at.% C) in cast/HIP condition and b) corresponding recalculated (0001)α_2 pole figure.

Fig. 13: Creep properties of cast/HIP TNM and TN1.5Mo-0.5C alloys at 780 °C and 150MPa. After 310 hours the creep tests were terminated. a) Evolution of creep strain with time and b) corresponding creep strain rate as function of creep strain.

Fig. 14: TEM bright-field images within the gauge volume of the TN1.5Mo-0.5C alloy after creep testing as shown in Fig. 13: a) Deformation-induced precipitation of fine p-type Ti_3AlC carbides at dislocations within the γ-phase (see arrow) and b) additional formation of coarse p-type carbides within the γ-phase of the α_2/γ-colonies due to the excess of C originating from the decreasing α_2-phase content and a reduced C-solubility within the γ-phase at testing conditions.

Fig_1

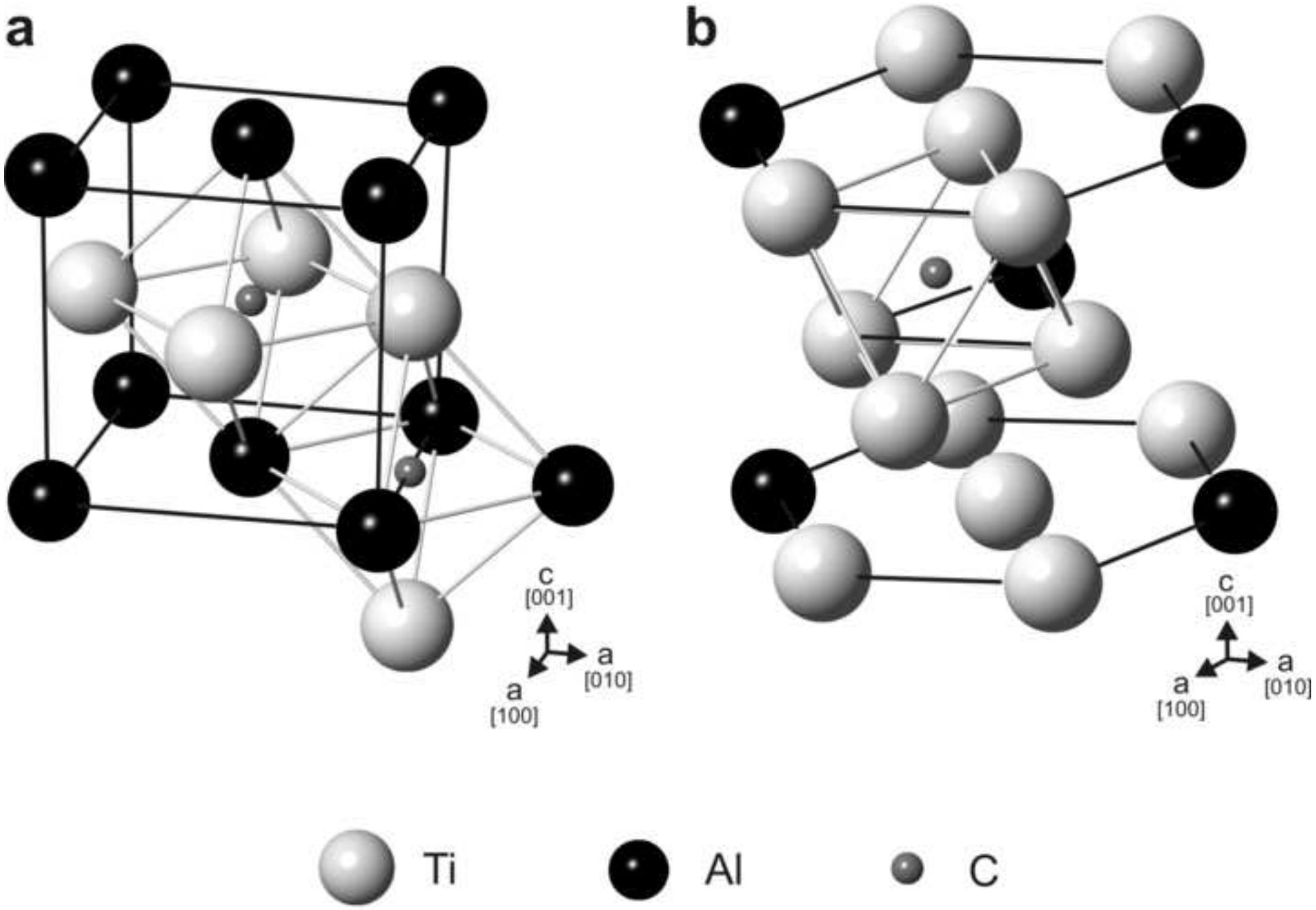

Fig_2

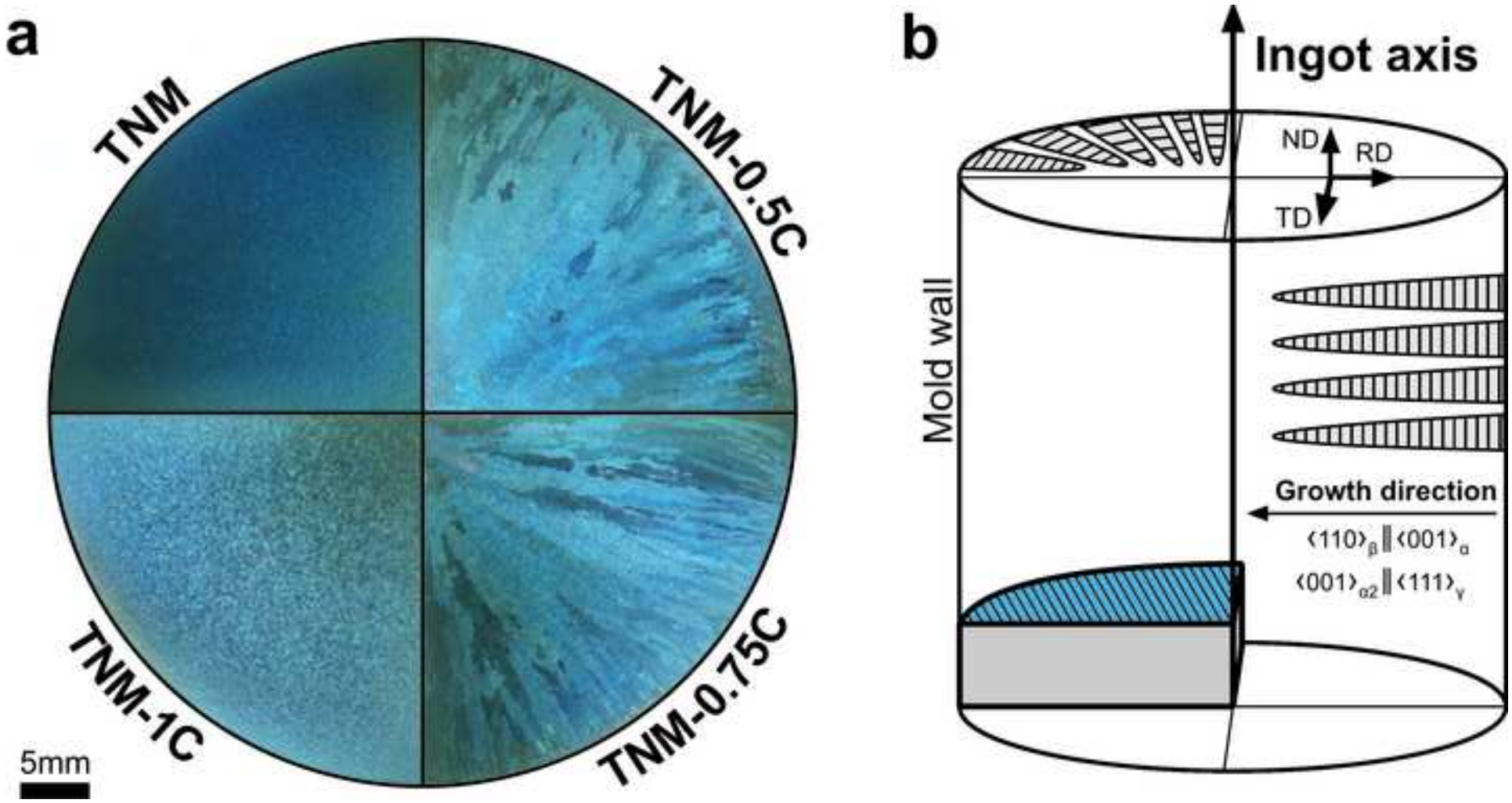
a
TNM
TNM-0.5C
TNM-1C
TNM-0.75C
5mm
b
Ingot axis
ND
RD
TD
Mold wall
Growth direction
⟨110⟩β ∥ ⟨001⟩α
⟨001⟩α2 ∥ ⟨111⟩γ

Fig_3

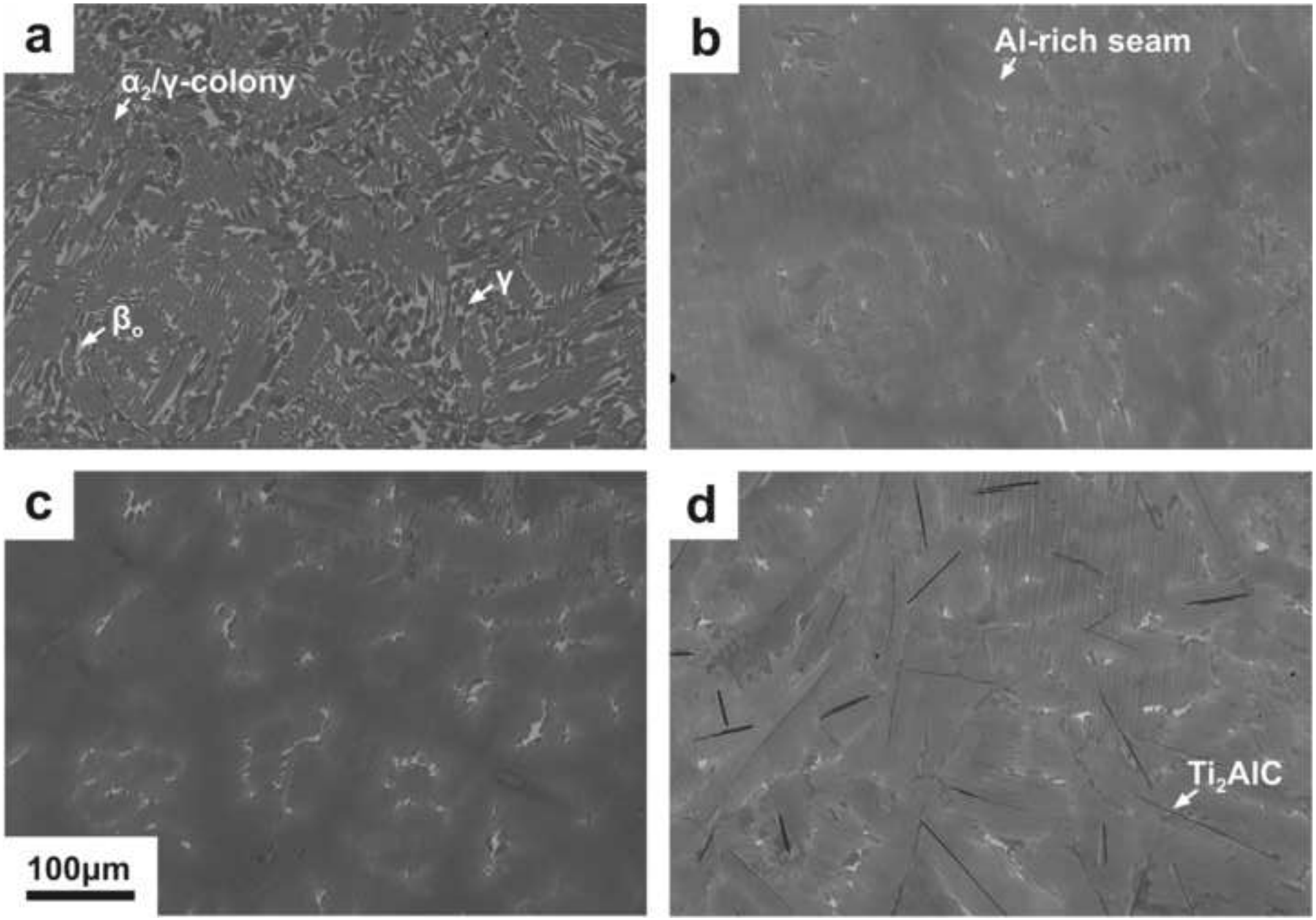
a
α_2/γ-colony
γ
β_o
b
Al-rich seam
c
100μm
d
Ti_2AlC

Fig_4

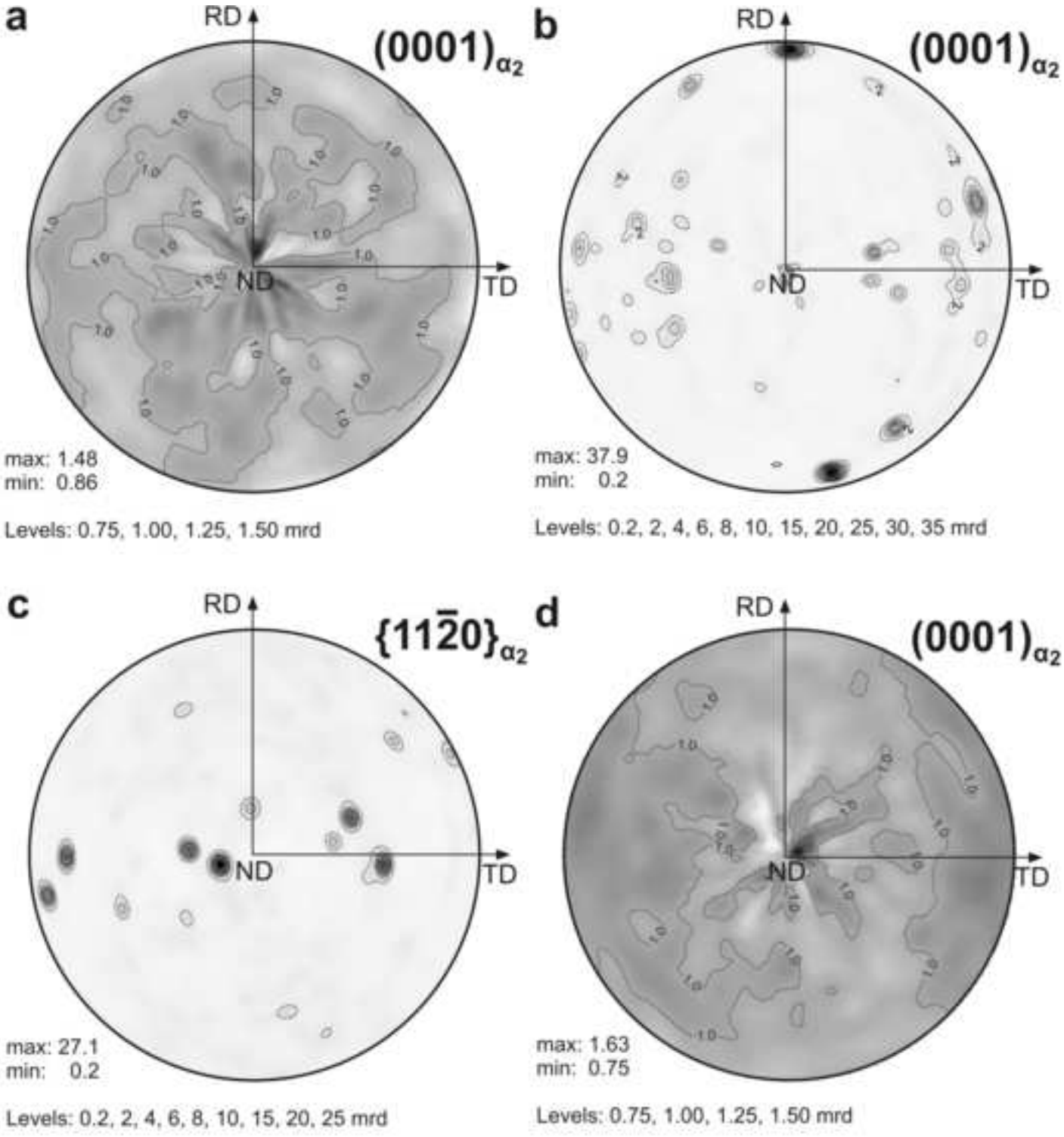
a
RD
$(0001)_{\alpha_2}$
ND
TD
max: 1.48
min: 0.86
Levels: 0.75, 1.00, 1.25, 1.50 mrd
b
RD
$(0001)_{\alpha_2}$
ND
TD
max: 37.9
min: 0.2
Levels: 0.2, 2, 4, 6, 8, 10, 15, 20, 25, 30, 35 mrd
c
RD
$\{11\bar{2}0\}_{\alpha_2}$
ND
TD
max: 27.1
min: 0.2
Levels: 0.2, 2, 4, 6, 8, 10, 15, 20, 25 mrd
d
RD
$(0001)_{\alpha_2}$
ND
TD
max: 1.63
min: 0.75
Levels: 0.75, 1.00, 1.25, 1.50 mrd

Fig_5

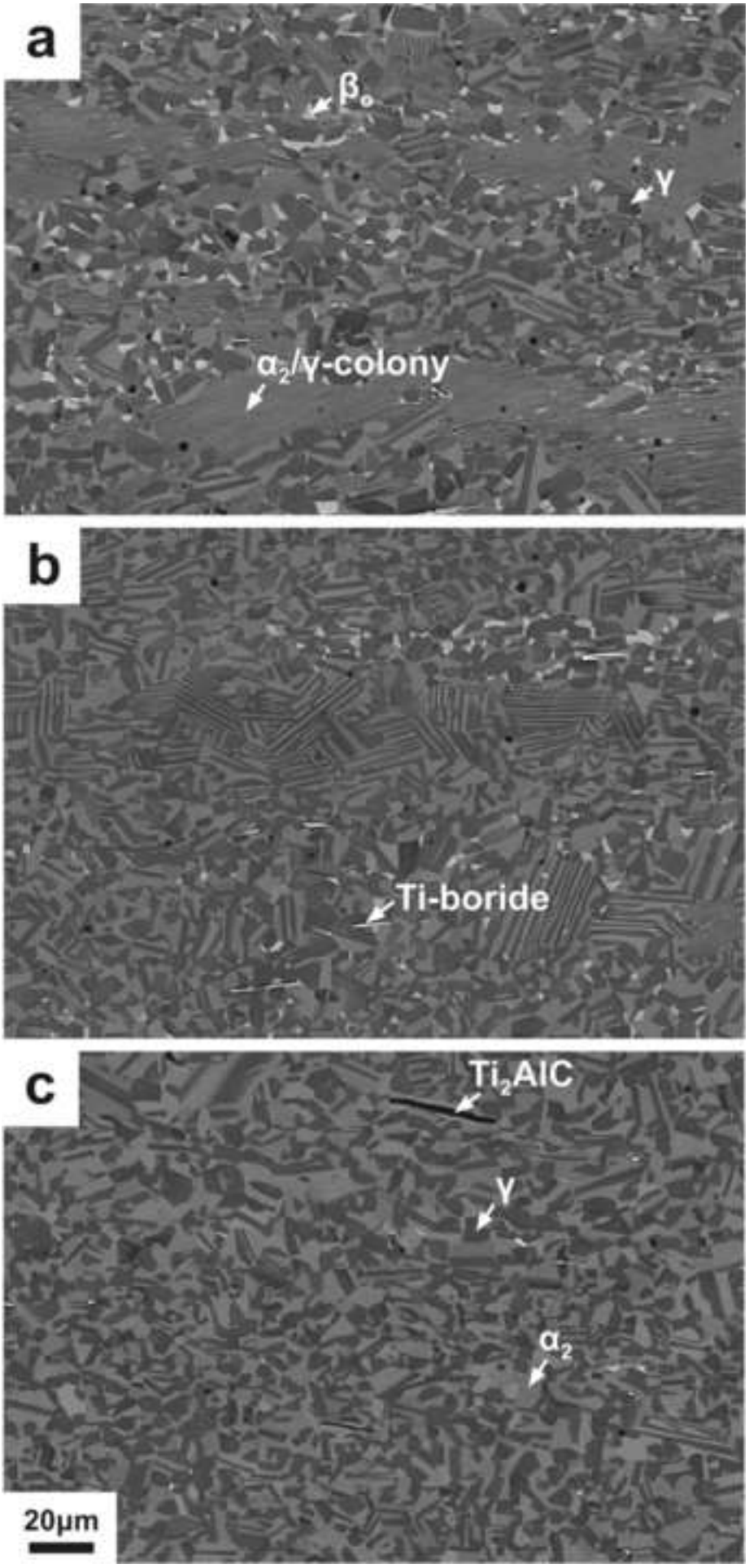

Fig_6

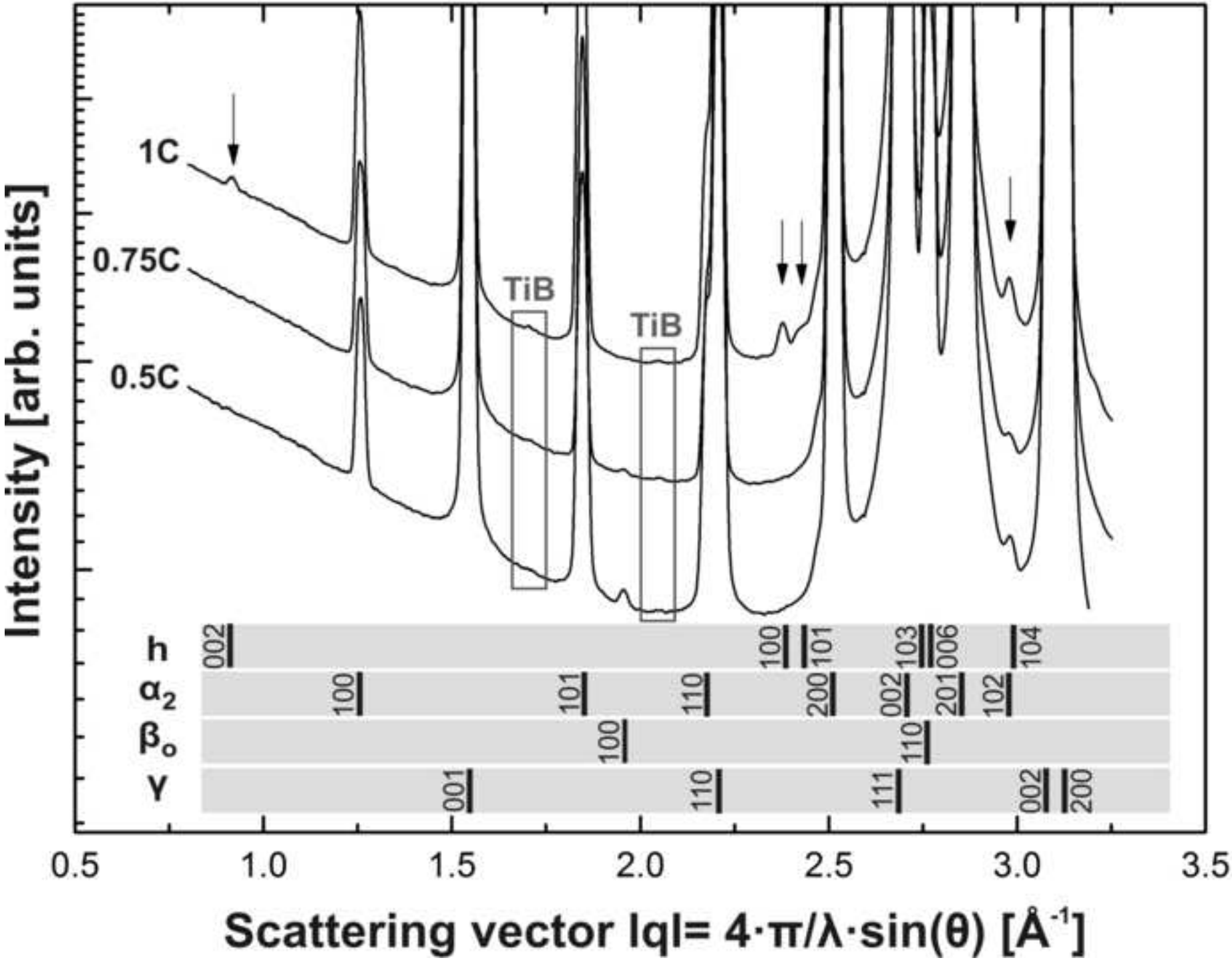
1C
0.75C
0.5C
TiB
TiB
Intensity [arb. units]
h
α2
βo
γ
002
100
101
110
200
002
201
006
102
103
104
100
100
110
001
110
111
002
200
0.5
1.0
1.5
2.0
2.5
3.0
3.5
Scattering vector |q|= 4·π/λ·sin(θ) [Å-1]

Fig_7

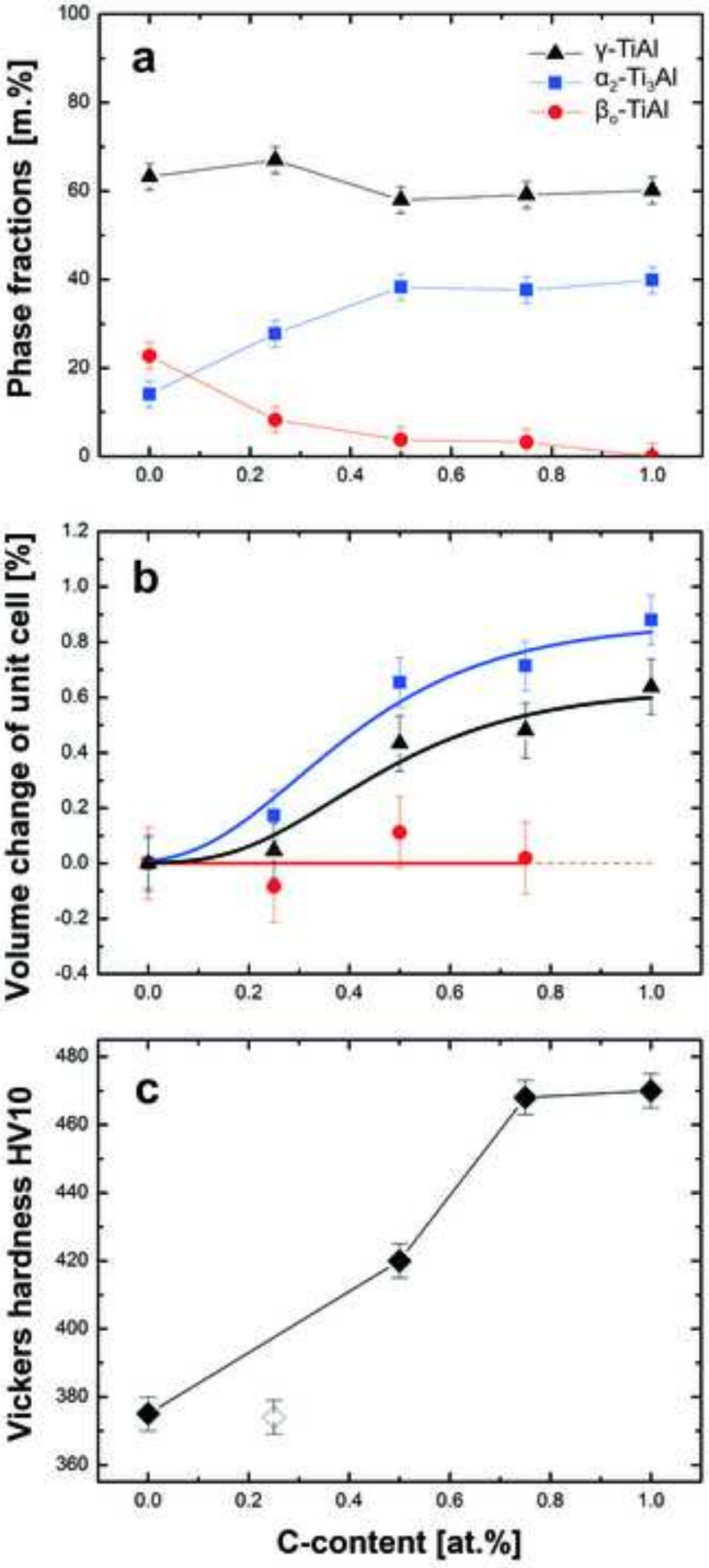
a
γ-TiAl
α2-Ti3Al
βo-TiAl
Phase fractions [m.%]
b
Volume change of unit cell [%]
c
Vickers hardness HV10
C-content [at.%]

Fig_8

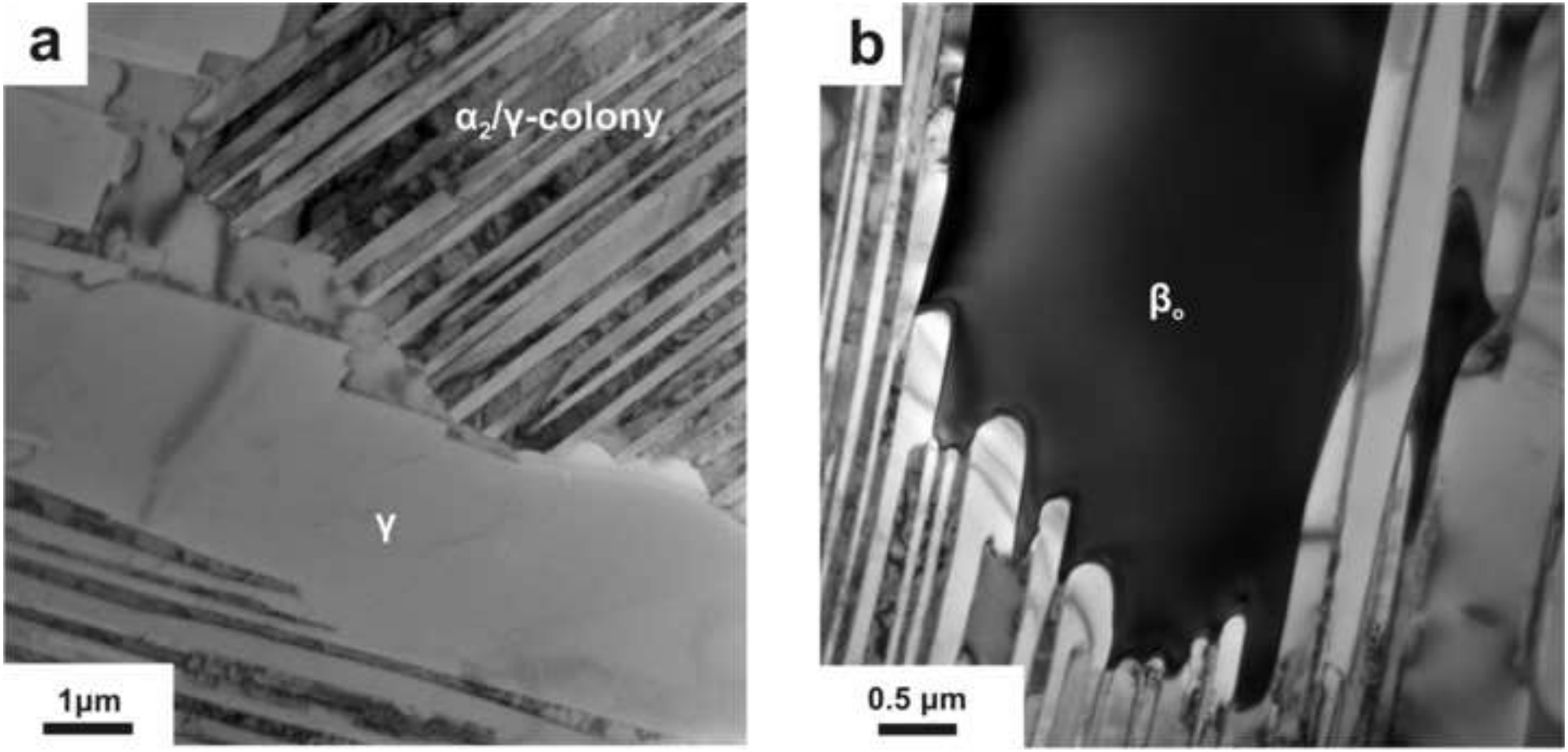

Fig_9

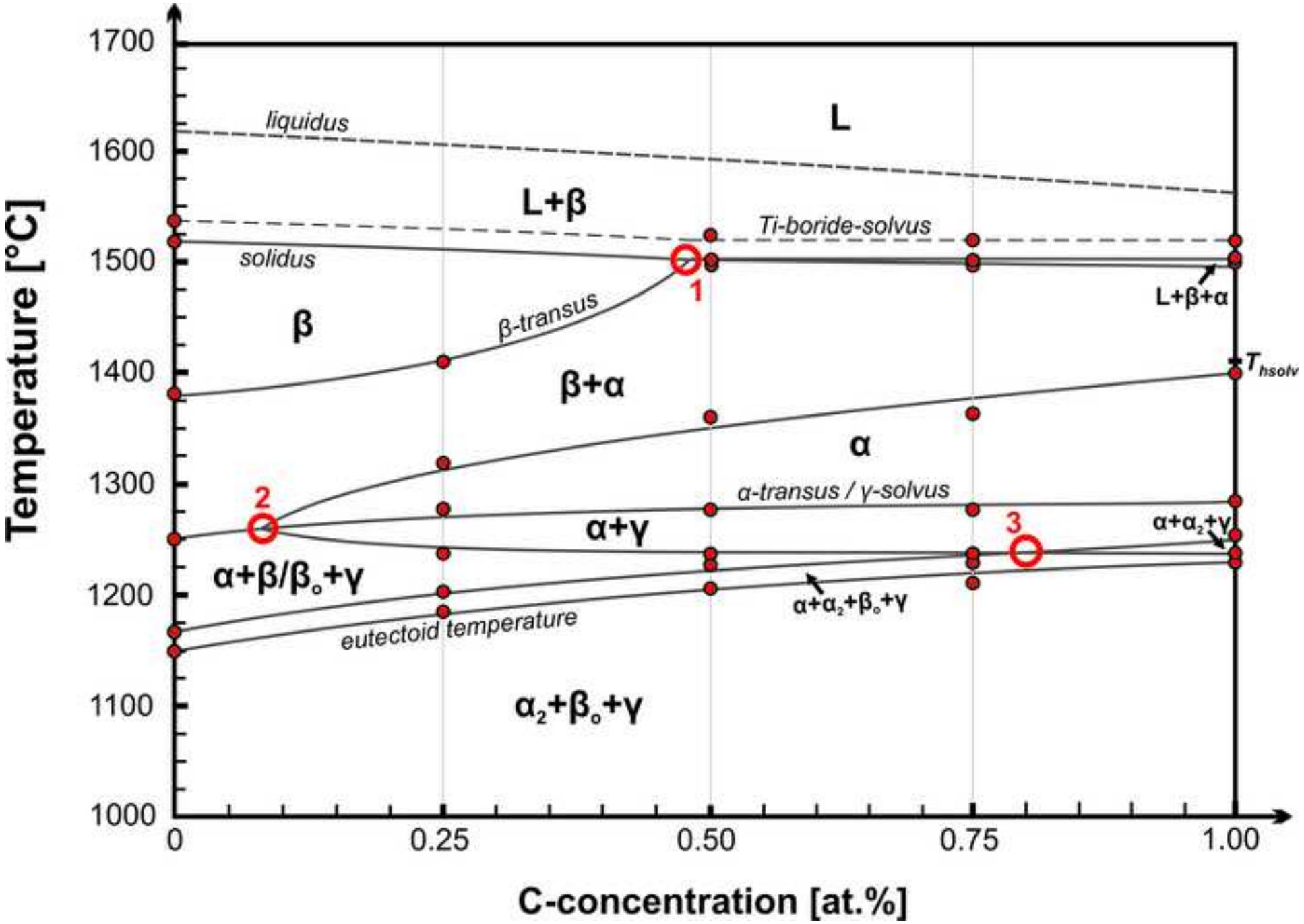
1700
1600
1500
1400
1300
1200
1100
1000
0
0.25
0.50
0.75
1.00
Temperature [°C]
C-concentration [at.%]
liquidus
L
L+β
Ti-boride-solvus
solidus
1
L+β+α
β
β-transus
β+α
T_{hsolv}
α
α-transus / γ-solvus
2
α+γ
3
α+α2+γ
α+β/β°+γ
α+α2+β°+γ
eutectoid temperature
α2+β°+γ

Fig_10

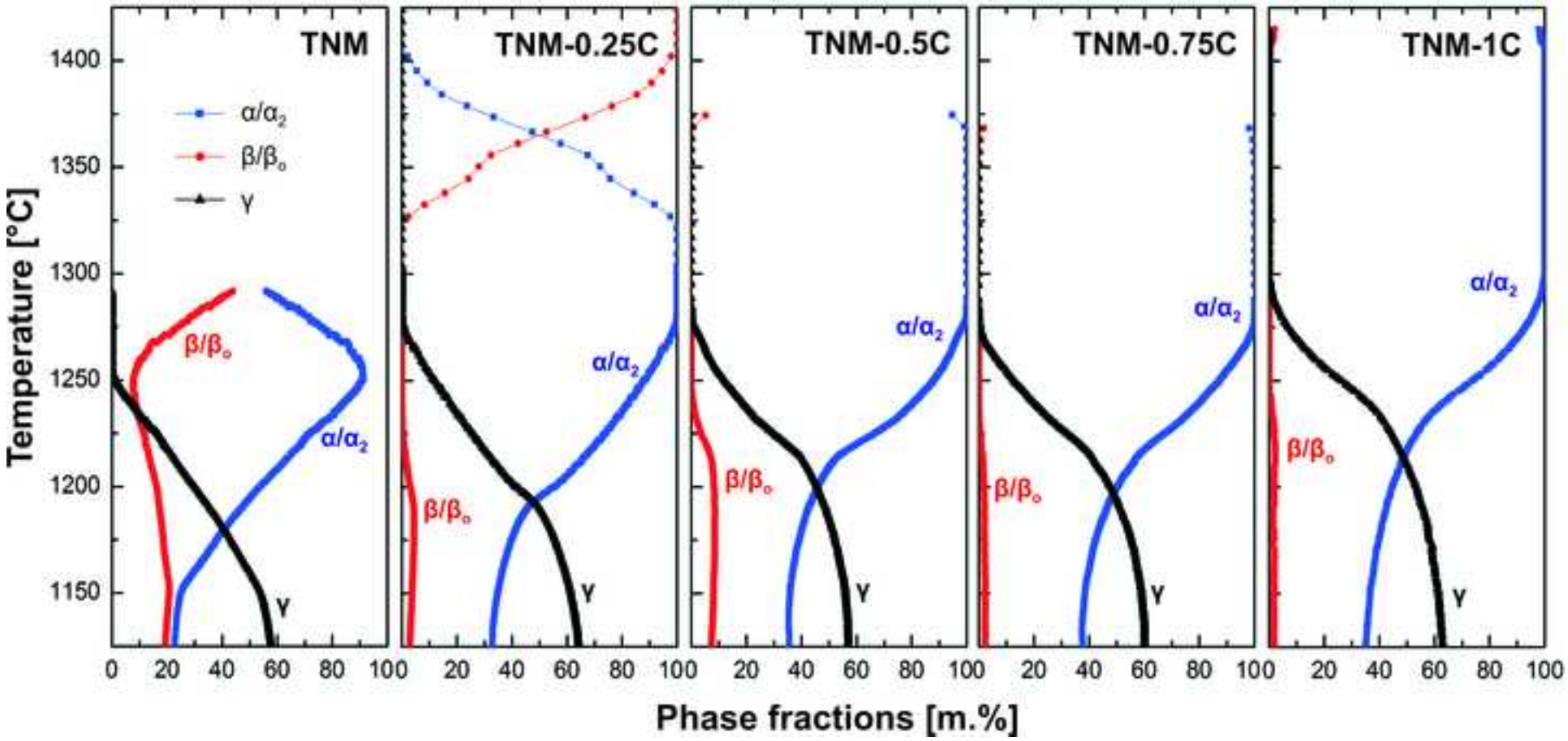
TNM
TNM-0.25C
TNM-0.5C
TNM-0.75C
TNM-1C
α/α2
β/βo
γ
Temperature [°C]
1400
1350
1300
1250
1200
1150
0
20
40
60
80
100
Phase fractions [m.%]

Fig_11

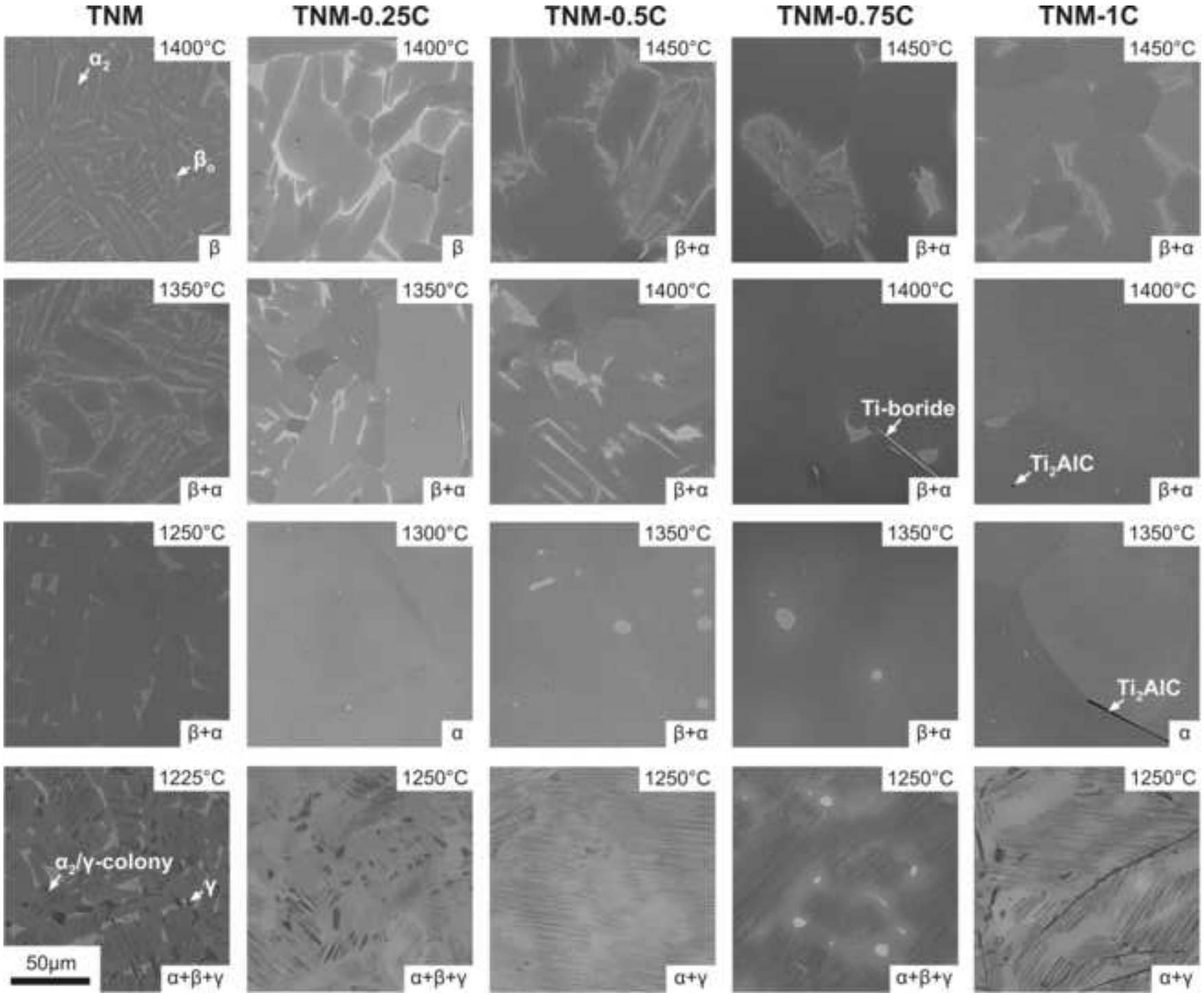
TNM
TNM-0.25C
TNM-0.5C
TNM-0.75C
TNM-1C
1400°C
1400°C
1450°C
1450°C
1450°C
α2
βo
β
β
β+α
β+α
β+α
1350°C
1350°C
1400°C
1400°C
1400°C
Ti-boride
Ti2AlC
β+α
β+α
β+α
β+α
β+α
1250°C
1300°C
1350°C
1350°C
1350°C
Ti2AlC
β+α
α
β+α
β+α
α
1225°C
1250°C
1250°C
1250°C
1250°C
α2/γ-colony
γ
50μm
α+β+γ
α+β+γ
α+γ
α+β+γ
α+γ

Fig_12

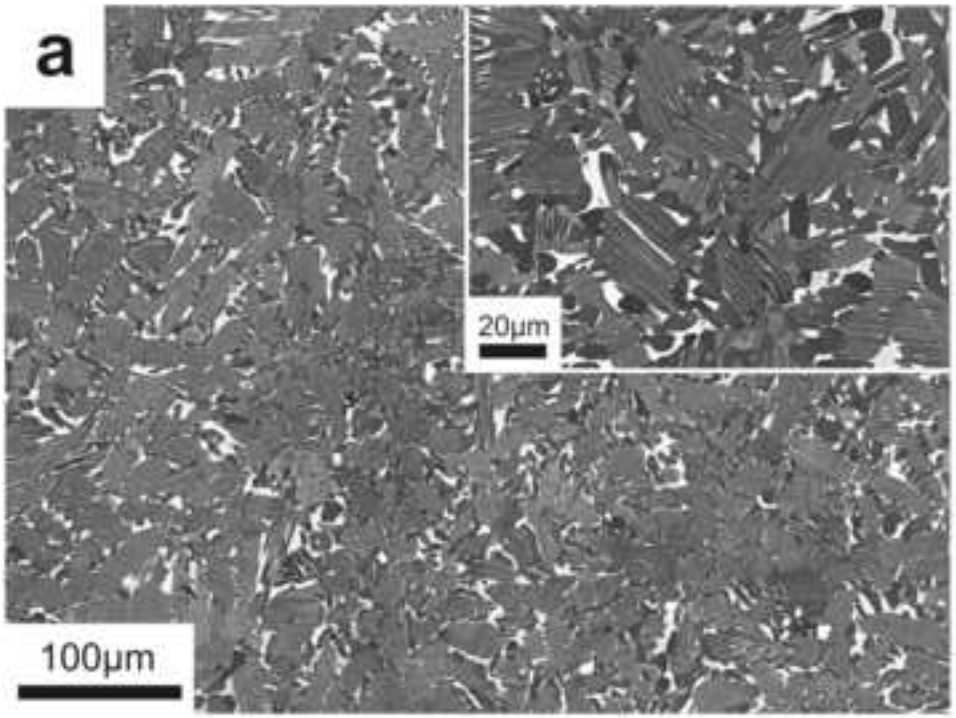

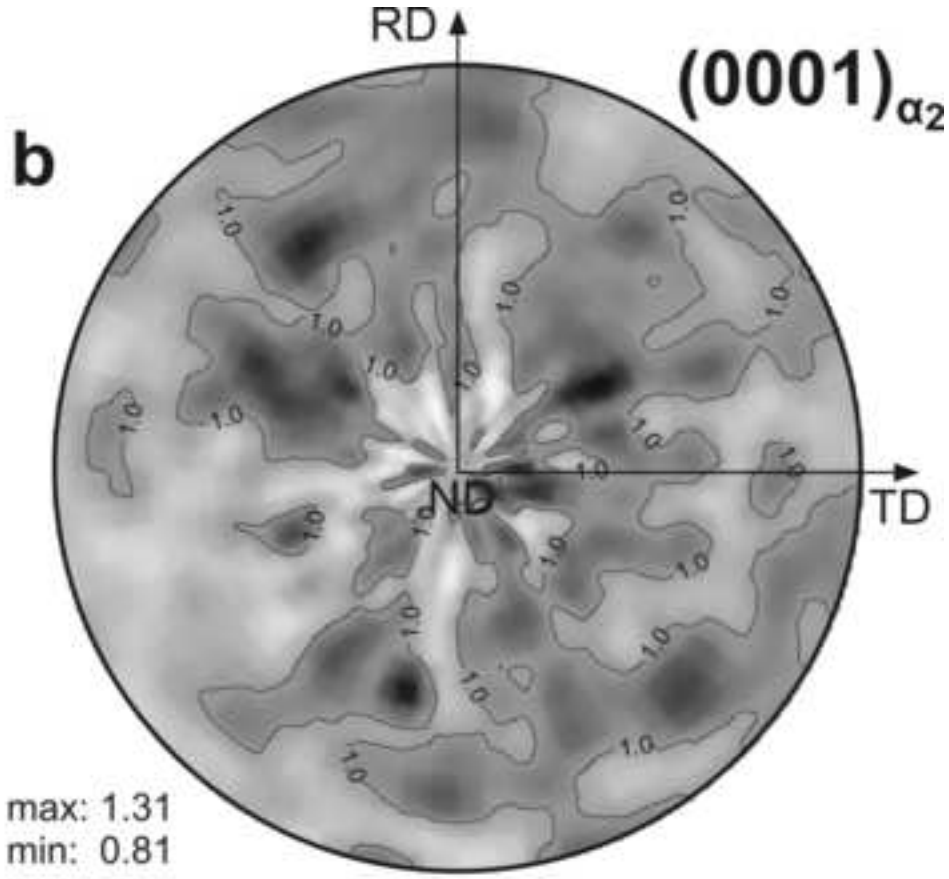

max: 1.31
min: 0.81

Levels: 0.75, 1.00, 1.25 mrd

Fig_13

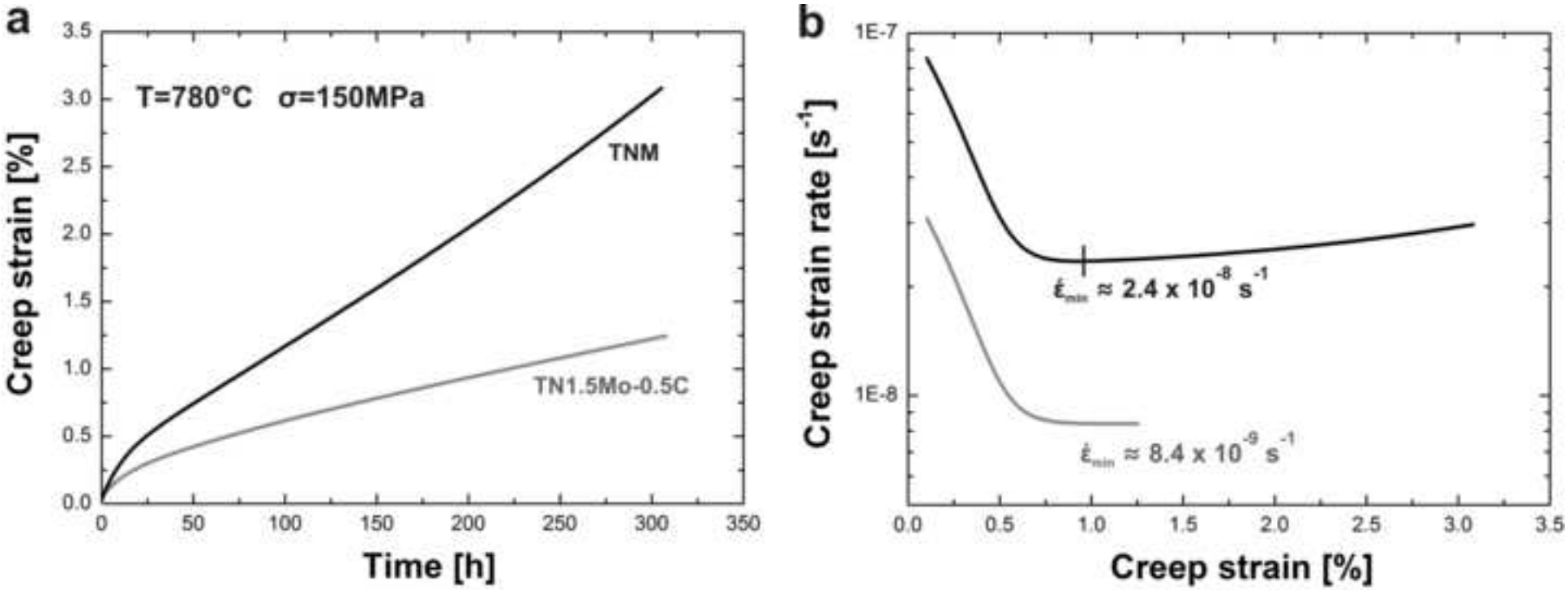
a
T=780°C σ=150MPa
TNM
TN1.5Mo-0.5C
Creep strain [%]
Time [h]
0.0
0.5
1.0
1.5
2.0
2.5
3.0
3.5
0
50
100
150
200
250
300
350
b
1E-7
1E-8
$\dot{\varepsilon}_{min} \approx 2.4 \times 10^{-8}\ s^{-1}$
$\dot{\varepsilon}_{min} \approx 8.4 \times 10^{-9}\ s^{-1}$
Creep strain rate [s^{-1}]
Creep strain [%]
0.0
0.5
1.0
1.5
2.0
2.5
3.0
3.5

Fig_14

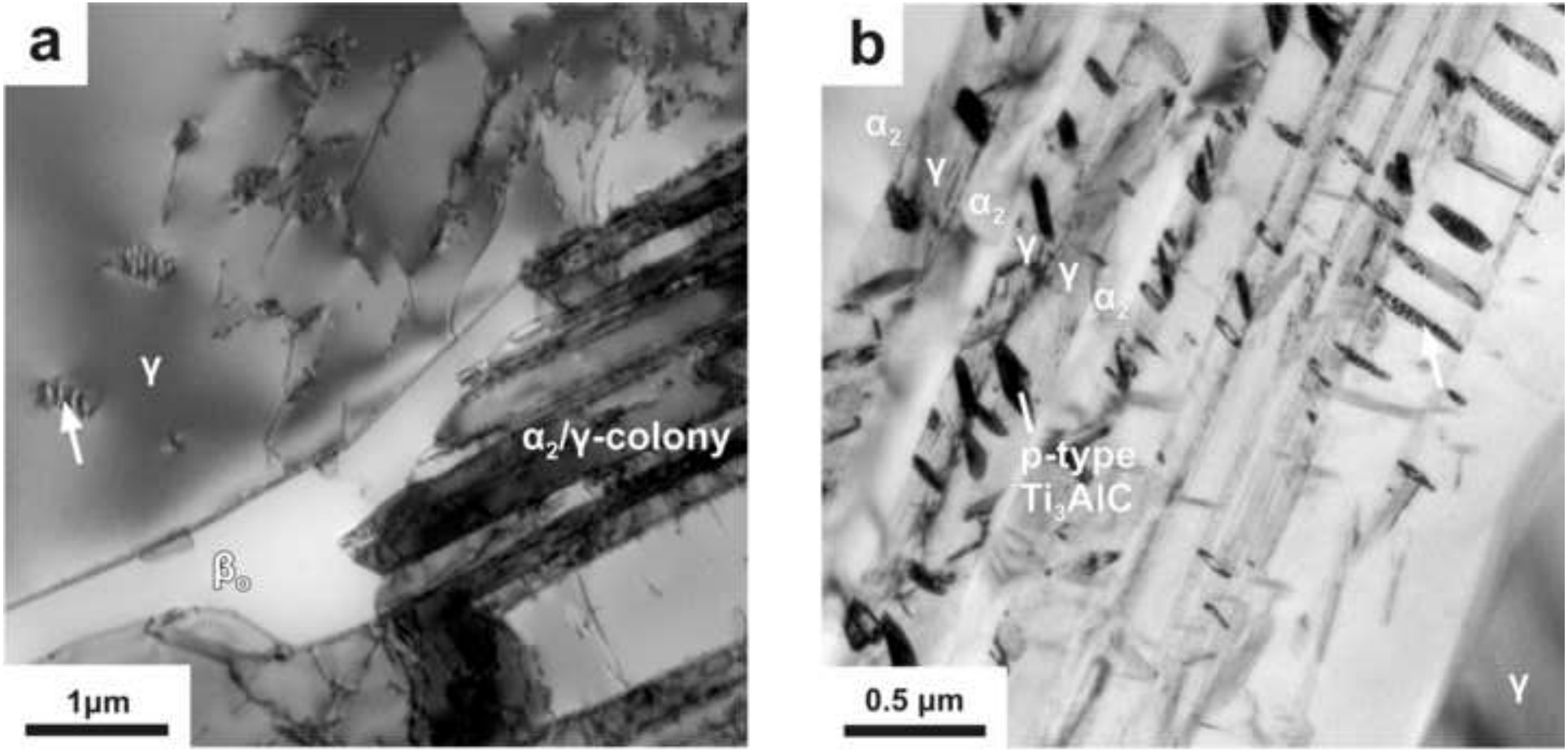

Table_1

Table 1: Chemical compositions of the investigated TNM-C alloys.

Alloy	Chemical composition [at.%] [1]					VAR	Melting, casting & processing
	Al	Nb	Mo	B	C		
TNM	43.20	3.99	1.01	0.09	–	2x	VAR skull + CC ingot + HIP
TNM-0.25C	43.52	4.00	0.94	0.11	0.21	4x	GC button + HIP-simulation
TNM-0.5C	43.72	4.13	1.05	0.11	0.51	1x	VIM skull + GC ingot + HIP
TNM-0.75C	43.68	4.11	1.05	0.11	0.78		
TNM-1C	43.35	4.06	1.02	0.11	1.02		
TN1.5Mo-0.5C	42.95	4.09	1.53	0.11	0.48	2x	VAR skull + CC ingot + HIP

[1] balance Ti; VAR = vacuum arc remelting; VIM = vacuum induction melting; CC = centrifugal casting; GC = gravity casting; HIP = hot-isostatic pressing (1200°C/4h/200MPa/FC); HIP-simulation = 1200°C/4h/FC